Investigating the Contribution of Collagen to the Tumor Biomechanical Phenotype with Non-invasive Magnetic Resonance Elastography

Jin Li[1*], Konstantinos Zormpas-Petridis[1*], Jessica K.R. Boult[1], Emma L. Reeves[1], Andreas Heindl[2], Maria Vinci[3¶], Filipa Lopes[4¶], Craig Cummings[1], Caroline J. Springer[4¶], Louis Chesler[5], Chris Jones[2], Jeffrey C. Bamber[1], Yinyin Yuan[2], Ralph Sinkus[6], Yann Jamin[1†] and Simon P. Robinson[1†]

Affiliations

[1]Division of Radiotherapy and Imaging, The Institute of Cancer Research, London, UK

[2]Division of Molecular Pathology, The Institute of Cancer Research, London, UK

[3] Bambino Gesù Children's Hospital-IRCCS, Rome, Italy, ¶previously Division of Molecular Pathology, The Institute of Cancer Research, London, UK

[4]Drug Discovery Unit Cancer Research UK Manchester Institute, University of Manchester, UK, ¶previously Cancer Therapeutics Unit, The Institute of Cancer Research, London, UK.

[5]Division of Clinical Studies, The Institute of Cancer Research, London, UK

[6]Division of Imaging Sciences and Biomedical Engineering, King's College London, UK

* These authors contributed equally to this work

† Co-senior authors and co-corresponding authors:

Dr. Yann Jamin
Division of Radiotherapy & Imaging
The Institute of Cancer Research,
15 Cotswold Road, Sutton
Surrey SM2 5NG, UK

Tel: 0208 722 4492
Fax: 0208 661 0846
e-mail: Yann.Jamin@icr.ac.uk

Dr. Simon P. Robinson
Division of Radiotherapy & Imaging
The Institute of Cancer Research,
15 Cotswold Road, Sutton
Surrey SM2 5NG, UK

Tel: 0208 722 4528
Fax: 0208 661 0846
e-mail: Simon.Robinson@icr.ac.uk

Research Article

Running title: Imaging tumor viscoelasticity with MR elastography

Keywords: preclinical elasticity imaging, MRI, stiffness, viscoelasticity, extracellular matrix, tumor mechanical phenotype, collagenase, mechanobiology

Financial support: European Union Horizon 2020 Research and Innovation Programme (Grant #668039), Cancer Research UK and EPSRC support to the Cancer Imaging Centre at ICR, in association with the MRC and Department of Health (England) (C1060/A10334 and C1060/A16464), The Rosetrees Trust (M593), support to SPR from Cancer Research UK Programme Grant (C16412/A27725), support from the Cancer Research UK Centre at the ICR, support to CJS from Wellcome Trust (grants WT1005X and 100282/Z/12/Z) & CTU at ICR (grant C309/A11566), support to LC from Cancer Research UK Programme Grants (C34648/A18339 and C34648/A14610). YJ and MV are Children with Cancer UK Research Fellows (2014/176 and 2016/234).

Conflict of interest: The authors have no conflict of interest to disclose

Word count: 4262

Number of tables: 0

Number of figures: 4

Abstract (241 words)

Increased stiffness in the extracellular matrix (ECM) contributes to tumor progression and metastasis. Therefore, stromal modulating therapies and accompanying biomarkers are being developed to target ECM stiffness. Magnetic resonance (MR) elastography can noninvasively and quantitatively map the viscoelastic properties of tumors *in vivo* and thus has clear clinical applications. Herein, we used MR elastography, coupled with computational histopathology, to interrogate the contribution of collagen to tumor biomechanical phenotype and evaluate its sensitivity to collagenase-induced stromal modulation. Elasticity (G_d) and viscosity (G_l) were significantly greater for orthotopic BT-474 (G_d=5.9±0.2kPa, G_l=4.7±0.2kPa, n=7) and luc-MDA-MB-231-LM2-4 (G_d=7.9±0.4kPa, G_l=6.0±0.2kPa, n=6) breast cancer xenografts, and luc-PANC1 (G_d=6.9±0.3kPa, G_l=6.2±0.2kPa, n=7) pancreatic cancer xenografts, compared to tumors associated with the nervous system, including GTML/*Trp53*$^{KI/KI}$ medulloblastoma (G_d=3.5±0.2kPa, G_l=2.3±0.2kPa, n=7), orthotopic luc-D-212-MG (G_d=3.5±0.2kPa, G_l=2.3±0.2kPa, n=7), luc-RG2 (G_d=3.5±0.2kPa, G_l=2.3±0.2kPa n=5) and luc-U-87-MG (G_d=3.5±0.2kPa, G_l=2.3±0.2kPa n=8) glioblastoma xenografts, intracranially propagated luc-MDA-MB-231-LM2-4 (G_d=3.7±0.2kPa, G_l=2.2±0.1kPa, n=7) breast cancer xenografts, and Th-*MYCN* neuroblastomas (G_d=3.5±0.2kPa, G_l=2.3±0.2kPa, n=5). Positive correlations between both elasticity (r=0.72, p<0.0001) and viscosity (r=0.78, p<0.0001) were determined with collagen fraction, but not with cellular or vascular density. Treatment with collagenase significantly reduced G_d (p=0.002) and G_l (p=0.0006) in orthotopic breast tumors. Texture analysis of extracted images of picrosirius red staining revealed significant negative correlations of entropy with G_d (r=-0.69, p<0.0001) and G_l (r=-0.76, p<0.0001), and positive correlations of fractal dimension with G_d (r=0.75, p<0.0001) and G_l (r=0.78, p<0.0001). MR elastography can thus provide sensitive imaging biomarkers of tumor collagen deposition and its therapeutic modulation.

Significance (17 words)

MR elastography enables non-invasive detection of tumor stiffness and will aid in the development of ECM-targeting therapies.

Introduction

Aberrant tensional homeostasis and increased stiffness are hallmarks of cancer. The origin of elevated tumor stiffness is not fully understood, but may often reflect increased mechanical stress associated with rapid tissue expansion and compressed vasculature and lymphatics, and extracellular matrix (ECM) rigidity. There is much evidence showing that increased tissue stiffness contributes to malignant transformation, tumor progression and metastasis (1,2). The elevated solid stress and interstitial fluid pressure (IFP) that may drive increased tumor stiffness are also two major obstacles to efficient tumor drug delivery (3).

Both breast and pancreatic cancers are characterized by excessive desmoplastic stromal reaction and dense ECM (4,5). Collagen, the principal component of the fibrillary protein network within the ECM, is the major contributor to ECM stiffening, is strongly implicated in tumor evolution and progression, and is associated with poor patient prognosis (6-9). Increased collagen deposition and enhanced matrix cross-linking occurs with progressive structural remodeling of the ECM scaffold which facilitates tumor growth (9). Suppression of collagen synthesis inhibits tumor growth and metastasis, and enhances drug penetration (10).

Significant efforts are currently focused on targeting tumor ECM stiffness for therapeutic gain (2,4,11-13). The development of stromal modulating therapies would benefit from non-invasive imaging biomarkers to inform on changes associated with therapeutic efficacy. A number of innovative magnetic resonance (MR) and ultrasound (US) imaging techniques are being exploited to image the viscoelastic and other mechanical properties of tissue *in vivo* (14-17). One approach, MR elastography, is being used to visualize and measure tissue elasticity and viscosity *in vivo*. MR elastography yields quantitative images, and therefore imaging biomarkers, that map the absolute value of the complex shear modulus G^* in terms of its two components, the elasticity modulus G_d (a measure of the ability of an object to resume a normal shape after being stretched or compressed) and the viscosity modulus G_l (a measure of resistance to gradual deformation by shear or tensile stress). We and others have demonstrated, in pre-clinical tumor models and cancer patients *in vivo*, the potential of the MR elastography-derived mechanical phenotype to inform on the underlying tumor microstructure and treatment-induced changes to its integrity (18-25).

Early imaging biomarker development demands close imaging-pathology correlation to understand the biological processes underpinning the imaging measurement, which can be meaningfully studied using animal models (26-28). The systematic evaluation of tumor

stromal components and their contribution to tissue stiffness as measured by MR elastography is in its infancy. This study describes the use of MR elastography, coupled with computational histopathology, to interrogate the contribution of the collagen network to the biomechanical phenotype imaged *in vivo* in a wide range of orthotopically-propagated and spontaneously arising transgenic models with disparate pathologies. The sensitivity of MR elastography to monitor stromal modulation *in vivo* following administration of collagenase is also demonstrated.

Materials and Methods

Cells

All cell lines used in this study tested negative for mycoplasma infection at the time of tumor implantation and human cells were authenticated by short tandem repeat (STR) profiling. Their origins, provenance and culture conditions are summarized in Supplementary Table 1 and 2.

Animals & Tumor Models

All animal experiments were approved by The Institute of Cancer Research Animal Welfare and Ethical Review Body, and performed in accordance with the UK Home Office Animals (Scientific Procedures) Act 1986, the United Kingdom National Cancer Research Institute guidelines for the welfare of animals in cancer research (29), and reported according to the ARRIVE (animal research: reporting *in vivo* experiments) guidelines (30). Mice were housed in specific pathogen-free rooms in autoclaved, aseptic microisolator cages with a maximum of 5 animals per cage. Mice were allowed access to sterile food and water *ad libitum*. A total of 84 mice were enrolled and a summary of the *in vivo* models used in this study is presented in Table 1.

Intracranial tumor propagation

Human luc-U-87 MG glioblastoma (5×10^4), rat luc-RG2 glioma (5×10^3), human luc-D-212 MG pediatric hemispheric giant-cell glioblastoma (5×10^3), or human metastatic luc-MDA-MB-231 LM2-4 breast cancer (5×10^3) cells were implanted supratentorially in the brains of adult female athymic NCr-*Foxn1*^{nu} mice (Charles River, Margate, UK) as previously described (19). Animals were anesthetized using 1-2% isoflurane in oxygen (1 l/min). A ~1 cm incision was made in the skin on the top of the head, and a 1mm hole drilled using a surgical bone microdrill (Harvard Apparatus, Edenbridge, UK). Cell suspension (5 µl) was then injected at a depth of 3 mm from the dura, at a rate of 2 µl/min, using a 10 µl syringe (VWR International, Lutterworth, UK) and a nanomite syringe pump (Harvard Apparatus). The needle was removed 3 minutes after completion of the injection and the skin repaired with Vetbond™ Tissue Adhesive (3M Animal Care Products, St Paul, MN, USA).

Tumor establishment and growth were monitored with bioluminescence imaging (BLI) using a Xenogen IVIS® 200 system coupled with LivingImage software (Caliper Life Sciences, Runcorn, UK). Luciferin (150mg/kg, Caliper Life Sciences) was administered intraperitoneally 10 minutes before imaging. MR elastography was performed when the BLI photon flux reached a threshold value previously determined to represent a tumor of

approximately 30-40 mm^3, a volume considered of sufficient size to acquire MR elastography data but not large enough to cause neurological effects in the mice. The average time from implantation to imaging was 18 days for the luc-U-87 MG and luc-MDA-MB-231 LM2-4 tumors, 22 days for the luc-RG2 tumors and 45 days for the luc-D-212 MG glioblastomas.

GTML/Trp53$^{KI/KI}$ transgenic model of medulloblastoma

The generation of the GTML/*Trp53*$^{KI/KI}$ mice has been previously reported (31). Mice were genotyped to detect the presence of human *MYCN* and *Trp53* transgenes. Male and female mice were monitored twice weekly for the development of a BLI signal from the midbrain. MR elastography was performed when the photon flux reached a threshold value previously determined to represent a tumor of approximately 20-30 mm^3.

Th-MYCN transgenic model of neuroblastoma

Transgenic Th-*MYCN* mice were genotyped to detect the presence of the human *MYCN* transgene (27). Both male and female hemizygous mice were used, which spontaneously developed palpable abdominal tumors between 50–130 days with a 25% penetrance. Tumor progression was monitored weekly by palpation by an experienced technician until the tumor reached a diameter greater than ~5 mm, at which point they underwent MR elastography.

Subcutaneous U87-MG xenografts

Adult female NCr-*Foxn1^{nu}* mice were injected subcutaneously in the flank with 2 x 10^6 luc-U-87-MG cells. Tumor development was monitored weekly by caliper measurements, and MR elastography performed when tumors reached a diameter of ~7 mm.

Orthotopic models of breast and pancreatic cancer

Human luc-MDA-MB-231 LM2-4 or BT-474 breast cancer cells (5 x 10^6) were injected into the third abdominal fat pad of adult female NCr-*Foxn1^{nu}* mice (100 µl cell suspension in PBS and matrigel (1:1)). A 17β-estradiol pellet (60-day release, Innovative Research of America, Sarasota, FL, USA) was implanted in the neck nape one day before implantation of BT-474 cells. Tumor development was monitored weekly by caliper measurements, and MR elastography performed when tumors reached a diameter of ~7 mm.

For the orthotopic propagation of pancreatic cancer xenografts, a small incision was made on the left flank of adult female athymic CD1-*Foxn1^{nu}* mice (Charles River, Margate, UK) through the skin and peritoneum, the pancreas exteriorized, and human luc-Panc-1 (1 x 10^7 cells in suspension in PBS and matrigel (1:1)) injected using a Hamilton syringe. The

pancreas was then returned into the abdominal cavity and the incision sutured. Successful engraftment and tumor progression were confirmed using BLI, and MR elastography performed ~90 days post-implantation.

Response to Collagenase

Orthotopic parental MDA-MB-231 and BT-474 breast cancer xenografts were propagated as described above. MR elastography was performed on established tumors 24 hours prior to and 5 hours after intravenous treatment with either collagenase (62U/kg, bacterial collagenase from *Clostridium histolyticum*, Sigma-Aldrich, UK) or saline.

MRI and MR elastography data acquisition and analysis

MRI was performed on a 7T horizontal bore MicroImaging system (Bruker, Ettlingen, Germany) using a 3cm birdcage volume coil. Tumor-bearing mice were anesthetized with a 10ml/kg intraperitoneal injection of fentanyl citrate (0.315mg/ml) plus fluanisone (10mg/ml (Hypnorm; Janssen Pharmaceutical Ltd., High Wycombe, UK)), midazolam (5mg/ml (Hypnovel; Roche)), and sterile water (used at a ratio of 1:1:2). The mouse core temperature was maintained at 37°C with warm air blown through the magnet bore.

Anatomical T_2-weighted images (using a rapid acquisition with refocused echoes (RARE) sequence, with TE = 36ms, TR = 4.5s, RARE factor = 8, 40 contiguous 1mm thick transverse slices, 1 average, matrix size 128×128 over a 3×3cm field of view (FOV)) were used to localize and determine the tumor volume, plan the MR elastography acquisition, and optimize the local field homogeneity over the region of interest (ROI) using the FASTMAP algorithm.

MR elastography was performed as previously described (18,19). The mechanical vibrations, generated by an electromagnetic shaker (Brüel & Kjaer, Nærum, Denmark), were transmitted through a flexible nylon rod to either *i)* a square piston with a concave curved face positioned on the mouse head for intracranial tumors, or directly on the skin over subcutaneous luc-U87-MG tumors and orthotopically propagated breast cancer xenografts, or *ii)* a round flat-faced piston placed on the abdomen above a palpated tumor (Th-*MYCN* or orthotopic pancreatic tumor*)*, all positioned within the volume coil at the isocenter of the magnetic field. MR elastography was performed using mechanical excitations at a vibration frequency of 1000 Hz, exciting the shaker with a voltage that generated mechanical waves inside the tumor with amplitude greater than 0.5 μm. A 2D spin-echo sequence incorporating sinusoidal motion-sensitizing gradients synchronized to the mechanical excitation was used. Data were acquired in 3 orthogonal directions, from 10 contiguous transverse slices (300 μm

thick), using 2 averages of 64 phase encoding steps over a 1.92×1.92 cm FOV, with TE = 27 ms, TR = 1001 ms and 8 time sampling steps, giving an isotropic spatial sampling of 300×300×300 μm of the mechanical wave propagation displacement inside the tumor. The total acquisition time was ~ 51 min. Finally, high resolution T_2-weighted RARE images were acquired from the same ten contiguous transverse slices, (TE = 36 ms, TR = 4.5 s, RARE factor = 8, 300 μm thick, 10 averages, matrix size 128×128 over a 1.92×1.92cm FOV).

*Image Reconstruction and Analysis***.** Parametric maps of the absolute value of the complex shear modulus |*G**|, elasticity G_d and viscosity G_l (where $|G^*| = G_d + iG_l$) were reconstructed using in-house software from the three-dimensional displacement vector measured as described above, and using the following equation (32):

$$-\rho\omega^2\vec{q} = G^*\nabla^2\vec{q}\,,\ \vec{q} = \vec{\nabla}\times\vec{u} \in C^3,$$

where $\vec{q}$ is the complex-valued curl of the measured displacement field $\vec{u}$, ρ is the density of the material and ω is the angular frequency. For each slice, G_d and G_l (kPa) were determined pixelwise from a ROI covering the whole tumor delineated from the high resolution T_2-weighted images.

Computational histopathology

Tissue preparation: Guided by the T_2-weighted MR images, tumors were carefully excised and orientated for subsequent histopathological processing. Adjacent formalin-fixed paraffin embedded sections (3 μm) were cut and tinctorially stained with picrosirius red (for collagen I and III), hematoxylin and eosin (H&E, for cellularity), or immunohistochemically processed for detection of the murine vascular endothelial marker CD31 (rabbit EP3095, Millipore, Watford, UK), using diaminobenzidine (DAB) as the chromogen.

Digitized histology: Whole-slide images were digitized using a NanoZoomer XR scanner (20x magnification, 0.46μm resolution, Hamamatsu, Japan). ROIs of viable tumor and necrosis for each sample were independently provided. Histology images were subsequently split into tiles of 2000x2000 pixels (jpeg).

Picrosirius red staining segmentation: A macro was written in Fiji (https://fiji.sc/) to segment picrosirius red staining from each tile using ImageJ/Fiji plugins (Java 8). Images were first converted from the RGB color space into the green-red (a*) color channel of the CIELAB color space (lightness, green–red and blue–yellow), and subsequently thresholded to segment the picrosirius red staining from the background. Following appraisal of automatic

and manual thresholding, two manual thresholds were chosen to achieve the optimal picrosirius red staining segmentation across all samples, whilst compensating for variations in staining intensity and complex background values associated with the different cancer pathologies. A threshold value of above +17 was used in the a* color channel for the majority of tumor types, increased to +23 for medulloblastomas and neuroblastomas arising in the GTML/*Trp53*$^{KI/KI}$ and Th-*MYCN* transgenic mice respectively, and subcutaneous luc-U-87-MG tumors. The segmentation algorithm was tested using independent annotation, from a single observer blinded to the algorithm's result, of stained/non-stained points (3920/3478) on 17 different samples across all cancer types, giving an accuracy of 95% with 91% sensitivity.

Cell segmentation from H&E-stained sections: Images were processed using the EBImage Bioconductor package (33). Cell nuclei were extracted from each image tile using the Otsu thresholding algorithm, followed by morphological opening to delete the noisy structures and the Watershed algorithm to separate clustered nuclei (34).

CD31 segmentation from CD31-stained immunohistochemistry sections: A macro was written in Fiji to extract DAB staining from each tile by applying color unmixing to extract the brown color channel, followed by application of the maximum entropy threshold detection method, both using ImageJ/Fiji plugins (Java 8) as previously described (27).

Generation of collagen fraction, cellularity and vascular density parametric maps: Whole-slide images of picrosirius red staining, segmented cells, and CD31 staining were converted into binary and processed to match MR elastography resolution (300x300µm), with the fraction of pixels occupied by the center of each cell nucleus, picrosirius red and CD31 staining within 664x664 pixel-regions representing a single pixel in the final calculated maps. Quantitative analysis of each stain was performed from one histological tumor section aligned with the central slice of the elastogram. Necrotic areas visible on both T_2-weighted images and corresponding histopathology slides were subtracted from the viable tumor by manual regional segmentation and excluded from the quantitative analysis.

Texture analysis: We evaluated the two-dimensional heterogeneity of collagen distribution by quantifying entropy and fractal dimension (FD), as described by Nieskoski et al (35), on the extracted collagen parametric maps. The texture analysis was implemented in Matlab (R2018b, Mathworks, Natick, MA, USA). Necrotic areas were subtracted from the viable tumor and excluded from the analysis. Entropy was quantified to measure the irregularity of collagen distribution by applying the "entropy" function of Matlab, which uses the equation:

$$Entropy = -\sum_{i=1}^{N} p * \log_2 p$$

, where p represents the normalized histogram count of the collagen fraction. FD defines the complexity (textural roughness) of collagen distribution within the tumor samples. The Hausdorff (box-counting) method was applied in the histology images within the 664x664 pixel-regions described earlier, using the equation:

$$FD = \log(N(e)) / \log(\frac{1}{e})$$

, where *e* represents the box size set to the size of the image and *N(e)* corresponds to the number of boxes of size 'e' which contain collagen. The median value of the generated FD maps (excluding necrotic areas) was used as the tumor's FD value.

Statistical Analysis

Statistical analysis was performed using GraphPad Prism 6 (GraphPad Software Inc., La Jolla, USA). Unless stated otherwise, data are presented as mean ± 1 s.e.m. Significant differences in quantitative MR elastography parameters between tumor types, and in relative treatment-induced changes, were identified using the non-parametric Mann-Whitney U-test with a 5% level of significance, whilst significant changes in MR elastography parameters with treatment were identified using the Wilcoxon matched-pairs signed ranks test with a 5% level of significance. Significant correlations were determined using linear regression analysis with a 5% level of significance using the robust regression and outlier removal approach (36).

Results

MR elastography was successfully performed in all mice, yielding an intertumoral coefficient of variation (CoV) of 13.0 and 15.4 % for repeated measurements of G_d and G_l respectively (Supplementary methods). MR elastography revealed a heterogeneous distribution of elasticity and viscosity across the nine orthotopic and transgenic models of cancer investigated (Figure 1A). Pronounced contrast between the established tumor and the surrounding brain was clearly evident in the intracranial models, with the lesion boundaries aligning with those seen in the high-resolution T_2-weighted images. Quantitative analysis of the MR elastography data demonstrated a wide range in G_d and G_l values across the models, from 3.5 ± 0.2 and 2.2 ± 0.2 kPa respectively in the GTML/*Trp53*$^{KI/KI}$ transgenic mouse model of medulloblastoma, to 7.9 ± 0.4 and 6.0 ± 0.2 kPa in the orthotopic luc-MDA-MB-231 LM2-4 mammary carcinomas (Figure 1B). Collectively, elasticity and viscosity were significantly ($p<0.0001$) greater for the orthotopically-propagated breast and pancreas models, compared to the tumors associated with the central or peripheral nervous system.

Intravenous injection of collagenase resulted in a clear overall reduction in the elasticity and viscosity of orthotopic MDA-MB-231 and BT-474 mammary tumors, as measured by MR elastography, 5 hours after administration (Figure 2A). Tumor regions exhibiting relatively high G_d and G_l pre-treatment were typically reduced following challenge with collagenase. No similar response was evident in the vehicle-treated mice. Collectively, collagenase resulted in a significant reduction in both G_d (6.0 ± 0.4 kPa to 4.9 ± 0.4 kPa, $p=0.001$) and G_l (3.8 ± 0.6 kPa to 3.0 ± 0.5 kPa, $p=0.001$), which was not observed in the vehicle-treated cohort (G_d: 5.1 ± 0.4 kPa to 5.4 ± 0.3 kPa, $p=0.3$; G_l: 3.0 ± 0.6 kPa to 3.4 ± 0.5 kPa, $p=0.13$). Relative changes in both G_d and G_l were significantly different between the collagenase and vehicle-treated cohorts ($p=0.0008$ and $p=0.0004$, Figure 2B).

To investigate the pathological determinants of the regional variations in tumor viscoelasticity seen *in vivo*, parametric maps of G_d and G_l were compared with maps of picrosirius red (collagen I & III), H&E (cellularity) and CD31 (vascular density) staining, automatically segmented from high-resolution images of aligned tissue sections from the same tumor (Figure 3A). In the the GTML/*Trp53*$^{KI/KI}$ transgenic mouse model, which exhibited the lowest mean G_d and G_l, of all the models investigated, tumors presented with a thin layer-like region of elevated G_d and G_l spatially associated with strong picrosirius red staining adjacent to the skull, consistent with tumor invasion into the collagen-rich meninges (Figure 3B). In general, but especially in breast and pancreatic tumors, regions demonstrating high values of G_d and G_l spatially corresponded to cellular regions with higher deposition of collagen. In some

tumors, histologically-defined regions of extensive tissue damage (e.g. necrosis) were spatially associated with areas of markedly lower elasticity and viscosity. It is important to note the relative softness of these necrotic regions irrespective of their also having high collagen content. These regions were excluded from the subsequent quantitative analysis. Quantitative analysis identified statistically significant positive inter-tumor correlations of both tumor-mean elasticity G_d (r=0.72, p<0.0001) and viscosity G_l (r=0.78, p<0.0001) with tumor-mean collagen fraction, but not with tumor-mean cellularity and vascular density (Figure 3C).

The irregularity of collagen distribution and deposition, and its relationship to tumor viscoelasticity *in vivo*, was further investigated using texture analysis of the extracted images of picrosirius red staining. Significant negative correlations of entropy with G_d (r=-0.69, p<0.0001) and G_l (r=-0.76, p<0.0001), and positive correlations of FD with G_d (r=0.75, p<0.0001) and G_l (r=0.78, p<0.0001) were found (Figure 4A and B). Entropy values close to zero and relatively high values of FD determined in the BT-474, luc-PANC-1 and luc-MDA-MB-231 LM2-4 tumors are consistent with the presence of a homogeneous and dense collagen network. Note that in the models investigated, increasing collagen content was associated with both increasing density and uniformity of its distribution, as shown by the mono-exponential relationship of entropy ($y= 3.86e^{-0.24x}$, $r^2=0.76$) and logarithmic relationship of FD ($y= 0.15\ln x + 1.16$, $r^2=0.98$) with collagen fraction, respectively (Figure 4C).

Discussion

ECM stiffening is increasingly recognized as a major mechanical signal, which alters cell behavior and in part confers to cancer cell hallmark capabilities including sustained growth, invasion and metastasis (6,7,37-42). ECM stiffening is also associated with increased solid stress and IFP, two other hallmarks of tumor mechanobiology that induce blood and lymphatic vessel compression, and reduced transcapillary transport respectively, and which impair effective drug delivery (3). Disrupting the crosstalk between cancer cells and the ECM, as well as reversing ECM stiffness, solid stress or IFP, thus represents a promising therapeutic strategy (11). The clinical development of stromal modulating therapies would be facilitated and accelerated by non-invasive imaging methods to longitudinally image and quantify tumor mechanical properties *in vivo* (15-17).

In this pre-clinical study, our quantitative MR elastography tumor data, combined with aligned computational histopathology, showed that elevated tumor G_d and G_l correlated with increased collagen deposition across a wide range of clinically-relevant tumor models with disparate pathologies. Our data particularly highlight the relative softness of tumors arising in the nervous system, and the predicted elevated stiffness of orthotopic breast and pancreatic models. Furthermore, modulation of the collagen network with bacterial collagenase in two relatively stiff orthotopic models of breast cancer reveal a marked reduction in both elasticity and viscosity. Collectively our results demonstrate that the deposition and density of the collagen fiber network is a major determinant of the tumor biomechanical phenotype, for which MR elastography provides sensitive *in vivo* imaging biomarkers, including biomarkers of its pharmacological modulation.

Our MR elastography study also aligns with several established concepts in tissue mechanics. The elastic properties of tissues are defined by the mechanical characteristics of their cells and their surrounding ECM, yet tissue macroscopic viscoelastic properties are not greatly affected by differences in cell morphology and density, but are largely governed by their ECM composition (43). Herein, histologically-confirmed regions of tissue damage (necrosis) were associated with markedly reduced elasticity and viscosity visualized *in vivo*. This relation is irrespective of the collagen fraction within the necrotic regions and explains the heterogeneous appearance of the viscoelastic maps, as well as the absence of spatial correspondence with the homogenous network of collagen in the luc-PANC-1 tumors, which exhibit marked and widespread regions of multifocal discrete necrosis. This is also consistent with previous MR elastography studies reporting a reduction in viscoelastic properties following vascular targeted-therapy induced cell death and/or reduction in

vascular density (18,20,21). Whilst this demonstrates the importance of both a viable cellular and vascular network to tissue integrity and mechanopathology, our data show they provide a very moderate contribution to the observed range of mechanical phenotypes, in contrast to differences in ECM characteristics.

Intracranial tumors were typically at the softer end of the spectrum of viscoelastic properties measured in this study (G_d ~4kPa and G_l ~2kPa) (19,22). The high compliance (inversely related to elastic modulus) of human brain tumors relative to the surrounding brain parenchyma has been reported, and in the case of glioblastoma, stiffness has been shown to decrease with tumor grade, measured as part of clinical MR elastography-embedded prospective studies (44,45). Brain tumors share the unique composition of the healthy brain, characterized by the absence of a fibrillar network (which resists shear deformation) and a reliance on hygroscopic hyaluronic acid (the main mechanical support against compressive forces that act to cause a change in volume but offer little resistance to shear) for mechanical support. The lack of collagen, a major facilitator of tumor cell intravasation, one of the earliest stages of metastasis, is consistent with the fact that intracranial tumors rarely disseminate outside the brain (46). Note also the relatively low viscoelastic properties of the intracranially grown luc-MDA-MB-231 LM2-4 tumors compared to those propagated in the mammary fat pad, highlighting the contribution of implantation site to the resulting biomechanical phenotype. Abdominal neuroblastomas spontaneously arising in Th-*MYCN* transgenic mice, and which are derived from the sympathetic nervous system, were also relatively soft with little collagen, consistent with their general clinical presentation (47). Interestingly, increased collagen III (reticulin) deposition helps to define an ultra-high-risk group of patients in which increased stiffness relates to metastatic potential, the major cause of mortality for children with neuroblastoma (48,49).

MR elastography revealed an acute reduction in breast tumor elasticity and viscosity following systemic administration of collagenase. A similar biomechanical response was recently reported following intratumoral injection of collagenase, measured using US-based elastography (16). Collagenase has also been shown to rapidly decrease tumor IFP in breast cancer xenografts (50,51). Cleavage of collagen with collagenase produces large peptide fragments which remain trapped within the ECM, making the acute effects of collagenase challenging to detect on conventional histology at such an acute time point (12). Having established their dependence on relative tumor collagen fraction, quantitation of tumor G_d and G_l can also provide early MRI biomarkers of response to collagen degradation *in vivo*. In this way, MR elastography could thus be exploited for monitoring direct enzymatic degradation of the ECM and/or targeted inhibition of collagen synthesis, potent strategies

being actively investigated to improve drug penetration in solid tumors, and showing promising results in clinical trials (10,12,52).

Solid stress has been shown to correlate with collagen deposition and be the major contributor to total tumor pressure in models of pancreatic cancer (53). ECM stiffening is a marker of poor prognosis in breast cancer and pancreatic ductal adenocarcinoma (6,37,38,40). Given its sensitivity to collagen deposition, MR elastography may thus potentially provide prognostic information, and through its sensitivity to collagen modulation, provide biomarkers of response to collagen-targeted approaches designed to alleviate solid stress for improved drug delivery. Tumor shear modulus, measured by US elastography, has been shown to positively correlate with collagen deposition and inversely correlate with functional vasculature and drug delivery (17). However, MR elastography cannot measure pressure directly, and as such may not be directly informative for strategies designed to decrease fluid stress (e.g. hyaluronidase), for which direct measurements of IFP are required. Reconstruction of tumor viscoelastic parameters from the properties of propagating waves or strain visualized by MRI or US has often used a simple monophasic linear viscoelastic mechanical model, which does not take in account any mobile fluid component (54). Measuring IFP and solid stress in itself represents a major clinical challenge, as current approaches for measuring both are invasive. Clinical measurement of IFP with wick-in-needles only permits very discrete sampling of the tissue and is unreliable, whilst innovative pre-clinical MRI methods shown to correlate with IFP *in vivo* would be difficult to routinely implement in a clinical setting (51,55).

Finally, the utility of MR elastography is being actively evaluated clinically in a wide range of health conditions including neuro- and cardiovascular pathologies, with applications including diagnosis, staging, surgical planning and intraoperative guidance. For example, the integration of MR elastography into the management of patients with chronic liver disease is now becoming well established for its excellent diagnostic accuracy, superior to that of US-based techniques, and ability to discriminate the different stages of liver fibrosis, characterized by increased deposition and crosslinking of collagen (56). Whilst less widely available and more costly than US-based techniques, MR elastography does allow the three dimensional investigation of large tissue areas and deep-seated organs. MR elastography can uniquely afford the non-invasive investigation of the mechanical properties of the brain and its pathology, including as recently demonstrated, neuronal activity (57). Lastly, MR elastography can be incorporated into multiparametric MR imaging protocols to enable comparison with other MRI-derived biomarkers of tumor structure and function in a single clinical scanning session.

In conclusion, we have shown that quantitation of elasticity G_d and viscosity G_l are sensitive imaging biomarkers of tumor collagen deposition, and response to direct enzymatic degradation of the collagen network. Given the importance of elevated ECM stiffness in tumor progression, and the continuing need for new technologies for faster and more accurate detection, diagnosis and monitoring, MR elastography has the potential to inform non-invasively on prognosis and improve risk stratification of cancer patients with dense stroma, and accelerate the development of stromal targeting/modulating treatment strategies.

References

1. Northey JJ, Przybyla L, Weaver VM. Tissue force programs cell fate and tumor aggression. Cancer Discovery **2017**;7:1224-37
2. Northcott JM, Dean IS, Mouw JK, Weaver VM. Feeling stress: the mechanics of cancer progression and aggression. Frontiers in Cell and Developmental Biology **2018**;6
3. Dewhirst MW, Secomb TW. Transport of drugs from blood vessels to tumour tissue. Nature reviews Cancer **2017**;17:738-50
4. Kota J, Hancock J, Kwon J, Korc M. Pancreatic cancer: Stroma and its current and emerging targeted therapies. Cancer letters **2017**;391:38-49
5. Conklin MW, Keely PJ. Why the stroma matters in breast cancer. Cell Adhesion & Migration **2012**;6:249-60
6. Provenzano PP, Inman DR, Eliceiri KW, Knittel JG, Yan L, Rueden CT*, et al.* Collagen density promotes mammary tumor initiation and progression. BMC medicine **2008**;6:11
7. Egeblad M, Rasch MG, Weaver VM. Dynamic interplay between the collagen scaffold and tumor evolution. Current opinion in cell biology **2010**;22:697-706
8. Fang M, Yuan J, Peng C, Li Y. Collagen as a double-edged sword in tumor progression. Tumour biology : the journal of the International Society for Oncodevelopmental Biology and Medicine **2014**;35:2871-82
9. Levental KR, Yu H, Kass L, Lakins JN, Egeblad M, Erler JT*, et al.* Matrix crosslinking forces tumor progression by enhancing integrin signaling. Cell **2009**;139:891-906
10. Liu J, Liao S, Diop-Frimpong B, Chen W, Goel S, Naxerova K*, et al.* TGF-β blockade improves the distribution and efficacy of therapeutics in breast carcinoma by normalizing the tumor stroma. Proceedings of the National Academy of Sciences **2012**;109:16618-23
11. Valkenburg KC, de Groot AE, Pienta KJ. Targeting the tumour stroma to improve cancer therapy. Nature reviews Clinical oncology **2018**;15:366-81
12. Dolor A, Szoka FC, Jr. Digesting a Path Forward: The Utility of Collagenase Tumor Treatment for Improved Drug Delivery. Mol Pharm **2018**;15:2069-83
13. Tang H, Leung L, Saturno G, Viros A, Smith D, Di Leva G*, et al.* Lysyl oxidase drives tumour progression by trapping EGF receptors at the cell surface. Nat Commun **2017**;8:14909
14. Mitchell MJ, Jain RK, Langer R. Engineering and physical sciences in oncology: challenges and opportunities. Nature reviews Cancer **2017**;17:659-75
15. Narunsky L, Oren R, Bochner F, Neeman M. Imaging aspects of the tumor stroma with therapeutic implications. Pharmacology & Therapeutics **2014**;141:192-208
16. Riegler J, Labyed Y, Rosenzweig S, Javinal V, Castiglioni A, Dominguez CX*, et al.* Tumor Elastography and Its Association with Collagen and the Tumor Microenvironment. Clin Cancer Res **2018**;24:4455-67
17. Wang H, Mislati R, Ahmed R, Vincent P, Nwabunwanne SF, Gunn JR*, et al.* Elastography Can Map the Local Inverse Relationship between Shear Modulus and Drug Delivery within the Pancreatic Ductal Adenocarcinoma Microenvironment. Clin Cancer Res **2018**
18. Li J, Jamin Y, Boult JKR, Cummings C, Waterton JC, Ulloa J*, et al.* Tumour biomechanical response to the vascular disrupting agent ZD6126 in vivo assessed by magnetic resonance elastography. British Journal of Cancer **2014**;110:1727-32
19. Jamin Y, Boult JKR, Li J, Popov S, Garteiser P, Ulloa JL*, et al.* Exploring the biomechanical properties of brain malignancies and their pathologic determinants in vivo with magnetic resonance elastography. Cancer Res **2015**;75:1216-24
20. Jugé L, Doan B-T, Seguin J, Albuquerque M, Larrat B, Mignet N*, et al.* Colon tumor growth and antivascular treatment in mice: complementary assessment with MR elastography and diffusion-weighted MR imaging. Radiology **2012**;264:436-44
21. Pepin KM, Chen J, Glaser KJ, Mariappan YK, Reuland B, Ziesmer S*, et al.* MR elastography derived shear stiffness—a new imaging biomarker for the assessment of early tumor response to chemotherapy. Magnetic Resonance in Medicine **2014**;71:1834-40
22. Feng Y, Clayton EH, Okamoto RJ, Engelbach J, Bayly PV, Garbow JR. A longitudinal magnetic resonance elastography study of murine brain tumors following radiation therapy. Physics in Medicine and Biology **2016**;61:6121
23. Garteiser P, Doblas S, Daire J-L, Wagner M, Leitao H, Vilgrain V*, et al.* MR elastography of liver tumours: value of viscoelastic properties for tumour characterisation. European Radiology **2012**;22:2169-77

24. Reiss-Zimmermann M, Streitberger K-J, Sack I, Braun J, Arlt F, Fritzsch D*, et al.* High resolution imaging of viscoelastic properties of intracranial tumours by multi-frequency magnetic resonance elastography. Clinical Neuroradiology **2015**;25:371-8
25. Bohte AE, Nelissen JL, Runge JH, Holub O, Lambert SA, de Graaf L*, et al.* Breast magnetic resonance elastography: a review of clinical work and future perspectives. NMR in Biomedicine **2018**;31:e3932
26. O'Connor JPB, Aboagye EO, Adams JE, Aerts HJWL, Barrington SF, Beer AJ*, et al.* Imaging biomarker roadmap for cancer studies. Nature reviews Clinical oncology **2017**;14:169-86
27. Zormpas-Petridis K, Jerome NP, Blackledge M, Carceller F, Poon E, Clarke M*, et al.* MRI imaging of the hemodynamic vasculature of neuroblastoma predicts response to anti-angiogenic treatment. Cancer Research **2019**;in press
28. Boult JKR, Jamin Y, Jacobs V, Gilmour LD, Walker-Samuel S, Halliday J*, et al.* False-negative MRI biomarkers of tumour response to targeted cancer therapeutics. British Journal of Cancer **2012**;106:1960-6
29. Workman P, Aboagye EO, Balkwill F, Balmain A, Bruder G, Chaplin DJ*, et al.* Guidelines for the welfare and use of animals in cancer research. Br J Cancer **2010**;102:1555-77
30. Kilkenny C, Browne WJ, Cuthill IC, Emerson M, Altman DG. Improving bioscience research reporting: the ARRIVE guidelines for reporting animal research. PLoS Biol **2010**;8:e1000412
31. Hill RM, Kuijper S, Lindsey JC, Petrie K, Schwalbe EC, Barker K*, et al.* Combined MYC and P53 defects emerge at medulloblastoma relapse and define rapidly progressive, therapeutically targetable disease. Cancer Cell **2015**;27:72-84
32. Sinkus R, Siegmann K, Xydeas T, Tanter M, Claussen C, Fink M. MR elastography of breast lesions: understanding the solid/liquid duality can improve the specificity of contrast-enhanced MR mammography. Magn Reson Med **2007**;58:1135-44
33. Pau G, Fuchs F, Sklyar O, Boutros M, Huber W. EBImage—an R package for image processing with applications to cellular phenotypes. Bioinformatics **2010**;26:979-81
34. Yuan Y, Failmezger H, Rueda OM, Ali HR, Gräf S, Chin S-F*, et al.* Quantitative image analysis of cellular heterogeneity in breast tumors complements genomic profiling. Science translational medicine **2012**;4:157ra43-ra43
35. Nieskoski MD, Marra K, Gunn JR, Hoopes PJ, Doyley MM, Hasan T*, et al.* Collagen Complexity Spatially Defines Microregions of Total Tissue Pressure in Pancreatic Cancer. Sci Rep **2017**;7:10093
36. Motulsky HJ, Brown RE. Detecting outliers when fitting data with nonlinear regression - a new method based on robust nonlinear regression and the false discovery rate. BMC bioinformatics **2006**;7:123
37. Acerbi I, Cassereau L, Dean I, Shi Q, Au A, Park C*, et al.* Human breast cancer invasion and aggression correlates with ECM stiffening and immune cell infiltration. Integrative Biology **2015**;7:1120-34
38. Armstrong T, Packham G, Murphy LB, Bateman AC, Conti JA, Fine DR*, et al.* Type I collagen promotes the malignant phenotype of pancreatic ductal adenocarcinoma. Clinical Cancer Research **2004**;10:7427-37
39. Schedin P, Keely PJ. Mammary gland ECM remodeling, stiffness, and mechanosignaling in normal development and tumor progression. Cold Spring Harbor perspectives in biology **2011**;3:a003228
40. Whatcott CJ, Diep CH, Jiang P, Watanabe A, LoBello J, Sima C*, et al.* Desmoplasia in primary tumors and metastatic lesions of pancreatic cancer. Clinical Cancer Research **2015**:clincanres. 1051.2014
41. Yu H, Mouw JK, Weaver VM. Forcing form and function: biomechanical regulation of tumor evolution. Trends in cell biology **2011**;21:47-56
42. Tadeo I, Berbegall AP, Castel V, Garcia-Miguel P, Callaghan R, Pahlman S*, et al.* Extracellular matrix composition defines an ultra-high-risk group of neuroblastoma within the high-risk patient cohort. Br J Cancer **2016**;115:480-9
43. de Schellenberger AA, Bergs J, Sack I, Taupitz M. The Extracellular Matrix as a Target for Biophysical and Molecular Magnetic Resonance Imaging. Quantification of Biophysical Parameters in Medical Imaging: Springer; 2018. p 123-50.
44. Pepin K, McGee K, Arani A, Lake D, Glaser K, Manduca A*, et al.* MR elastography analysis of glioma stiffness and IDH1-mutation status. American Journal of Neuroradiology **2018**;39:31-6
45. Simon M, Guo J, Papazoglou S, Scholand-Engler H, Erdmann C, Melchert U*, et al.* Non-invasive characterization of intracranial tumors by magnetic resonance elastography. New Journal of Physics **2013**;15:085024

46. Han W, Chen S, Yuan W, Fan Q, Tian J, Wang X*, et al.* Oriented collagen fibers direct tumor cell intravasation. Proc Natl Acad Sci U S A **2016**;113:11208-13
47. Braekeveldt N, Wigerup C, Tadeo I, Beckman S, Sanden C, Jonsson J*, et al.* Neuroblastoma patient-derived orthotopic xenografts reflect the microenvironmental hallmarks of aggressive patient tumours. Cancer Lett **2016**;375:384-9
48. Tadeo I, Piqueras M, Montaner D, Villamon E, Berbegall AP, Canete A*, et al.* Quantitative modeling of clinical, cellular, and extracellular matrix variables suggest prognostic indicators in cancer: a model in neuroblastoma. Pediatr Res **2014**;75:302-14
49. Zhu S, Zhang X, Weichert-Leahey N, Dong Z, Zhang C, Lopez G*, et al.* LMO1 Synergizes with MYCN to Promote Neuroblastoma Initiation and Metastasis. Cancer Cell **2017**;32:310-23 e5
50. Eikenes L, Bruland OS, Brekken C, Davies Cde L. Collagenase increases the transcapillary pressure gradient and improves the uptake and distribution of monoclonal antibodies in human osteosarcoma xenografts. Cancer Res **2004**;64:4768-73
51. Hassid Y, Eyal E, Margalit R, Furman-Haran E, Degani H. Non-invasive imaging of barriers to drug delivery in tumors. Microvasc Res **2008**;76:94-103
52. Murphy JE, Wo JY-L, Ryan DP, Jiang W, Yeap BY, Duda GD*, et al.* Potentially curative combination of TGF-b1 inhibitor losartan and FOLFIRINOX (FFX) for locally advanced pancreatic cancer (LAPC): R0 resection rates and preliminary survival data from a prospective phase II study. Journal of Clinical Oncology **2018**;36:4116-
53. Nieskoski MD, Marra K, Gunn JR, Kanick SC, Doyley MM, Hasan T*, et al.* Separation of Solid Stress From Interstitial Fluid Pressure in Pancreas Cancer Correlates With Collagen Area Fraction. J Biomech Eng **2017**;139
54. Nia HT, Liu H, Seano G, Datta M, Jones D, Rahbari N*, et al.* Solid stress and elastic energy as measures of tumour mechanopathology. Nat Biomed Eng **2016**;1
55. Walker-Samuel S, Roberts TA, Ramasawmy R, Burrell JS, Johnson SP, Siow BM*, et al.* Investigating Low-Velocity Fluid Flow in Tumors with Convection-MRI. Cancer Res **2018**;78:1859-72
56. Kennedy P, Wagner M, Castera L, Hong CW, Johnson CL, Sirlin CB*, et al.* Quantitative Elastography Methods in Liver Disease: Current Evidence and Future Directions. Radiology **2018**;286:738-63
57. Patz S, Fovargue D, Schregel K, Nazari N, Palotai M, Barbone PE*, et al.* Imaging localized neuronal activity at fast time scales through biomechanics. Sci Adv **2019**;5:eaav3816

Table 1. Summary of the *in vivo* models

Cell line	Characteristics	Study	Injection route	cells injected	n	Tumor volume (mm^3)*
luc-MDA-MB-231 LM2–4	Highly malignant human triple negative breast cancer cells isolated from a lung metastasis	MRE-histology correlation	**i.c.**	5×10^3	5	29 ± 8
		MRE-histology correlation	**o.t.**	2×10^6	6	406 ± 47
luc-RG2	Rat glioma cells	MRE-histology correlation	**o.t.**	5×10^3	5	30 ± 4
luc-U-87 MG	Human glioblastoma cells	MRE-histology correlation	**i.c.**	5×10^4	8	26 ± 4
		MRE-histology correlation	**s.c**	3×10^6	6	616 ± 114
luc-D-212 MG	Derived from a pediatric hemispheric giant-cell glioblastoma	MRE-histology correlation	**i.c.**	1.5×10^5	7	12 ± 3
MDA-MB-231	Highly malignant human triple negative breast cancer cells	Collagenase treatment	**o.t.**	2×10^6	14	385 ± 49
BT-474	Invasive ductal breast carcinoma cells	MRE-histology correlation	**o.t.**	5×10^6	7	438 ± 36
		Collagenase treatment	**o.t.**	5×10^6	7	287 ± 50.8
luc-PANC-1	Pancreatic epithelioid carcinoma cells	MRE-histology correlation	**o.t.**	1×10^7	7	1402 ± 280
Transgenic mouse models						
Th-*MYCN*	High-risk neuroblastoma	MRE-histology correlation	Spontaneously arising tumors		5	1369 ± 254
GTML/*Trp53*$^{KI/I}$	Medulloblastoma	MRE-histology correlation	Spontaneously arising tumors		7	27 ± 4

*Tumor volumes at the time of the MR elastography experiment and determined using segmentation from regions of interest drawn on each tumor-containing T_2-weighted MRI slice. i.c. intracranial, o.t. orthotopic, s.c. subcutaneous

Figure legends

Figure 1. MR elastography reveals marked differences in viscoelasticity measured *in vivo* in orthotopic and transgenic models of cancer. (**A**) Representative T_2-weighted MRI and associated parametric maps of elasticity G_d and viscosity G_l obtained from a medulloblastoma spontaneously arising in the brain of a GTML/*Trp53*$^{KI/KI}$ transgenic mouse (n=7), intracranially (i.c.) propagated luc-MDA-MB-231 LM2-4 breast cancer (n=5) and luc-D-212-MG glioblastoma xenografts (n=7), a neuroblastoma spontaneously arising in a Th-*MYCN* transgenic mouse (n=5), intracranially propagated luc-RG2 (n=5) and luc-U-87 MG glioblastoma xenografts (n=8), and orthotopic BT-474 breast cancer (n=7), luc-PANC1 pancreatic cancer (n=7) and luc-MDA-MB-231 LM2-4 breast cancer (n=6) xenografts. The dashed line (---) indicates the tumor boundaries defined on T_2-weighted images. (**B**) Quantitative summary of mean of the mean tumor G_d and G_l (± 1 s.e.m) for each model. The insets show that the collective average of G_d and G_l determined in the breast and pancreatic tumors was significantly higher than in tumors arising in the nervous system (****p<0.0001).

Figure 2. MR elastography can inform on tumor stromal modulation induced by collagenase. (**A**) Representative T_2-weighted anatomical MRI images, and parametric maps of G_d and G_l, acquired from mice bearing orthotopic BT-474 breast cancer xenografts 24 hours prior to and 5 hours after intravenous injection of either vehicle or collagenase. (**B**) Relative changes (%) in tumor median G_d and G_l measured in orthotopic MDA-MB-231 (blue symbols) and BT-474 (red symbols) breast cancer xenografts measured 5 hours after administration of either vehicle (○) or collagenase (△). Data are the individual changes from each tumor, and the combined cohort mean ± 1 s.e.m. Collagenase induced a significant reduction in both G_d and G_l compared to vehicle control.

Figure 3. MR elastography-derived elasticity G_d and viscosity G_l correlate with tumor collagen fraction. Representative anatomical T_2-weighted MRI images and parametric maps of elasticity (G_d) and viscosity (G_l), and the corresponding computed maps of picrosirius red staining (collagen I & III), hematoxylin and eosin staining (cellularity) and immunohistochemical detection of Cd31 (vascular density) extracted from high-resolution images of tissue sections from: (**A**) a medulloblastoma spontaneously arising in the brain of a GTML/*Trp53*$^{KI/KI}$ transgenic mouse, a neuroblastoma spontaneously arising in a Th-*MYCN*

transgenic mouse, and an intracranially propagated luc-U87-MG glioblastoma xenograft, and (**B)** from orthotopic BT-474, luc-PANC-1 and luc-MDA-MB-231 LM2-4 breast and pancreatic cancer xenografts. Note that the areas above the brain tumors showing both high viscoelastic properties and high picrosirius red staining correspond to regions where the tumor has invaded the collagen-rich meninges. Dotted lines indicate regions of necrosis. Note that in necrotic areas, high collagen density is not associated with high value of G_d and G_l. **(C)** Scatter graphs of individual tumor mean G_d and G_l plotted against mean collagen fraction (%), cellularity and vessel density. Linear regression analysis and 95% confidence intervals for significant correlations are shown.

Figure 4. The relationship between MR elastography-derived tumor viscoelastic properties and the spatial distribution and deposition of collagen evaluated by texture analysis. Scatter graphs of individual mean tumor elasticity G_d and viscosity G_l plotted against (**A**) entropy and (**B**) fractal dimension (FD). Linear regression analysis and 95% confidence intervals for significant correlations are shown. Note that both G_d and G_l are negatively correlated with entropy and positively correlated with FD, indicating that increased tumor stiffness is associated with more complex and more homogenously distributed collagen. Entropy values close to zero and relatively high values of FD determined in the BT-474, luc-PANC-1 and luc-MDA-MB-231 LM2-4 tumors are consistent with the presence of such a homogeneous and dense collagen network. (**C**) Scatter graphs showing the mono-exponential relationship between entropy and collagen fraction ($y= 3.86e^{-0.24x}$, $r^2=0.76$), and logarithmic relationship between fractal dimension and collagen fraction ($y= 0.15\ln x + 1.16$, $r^2=0.98$).

Figure 1

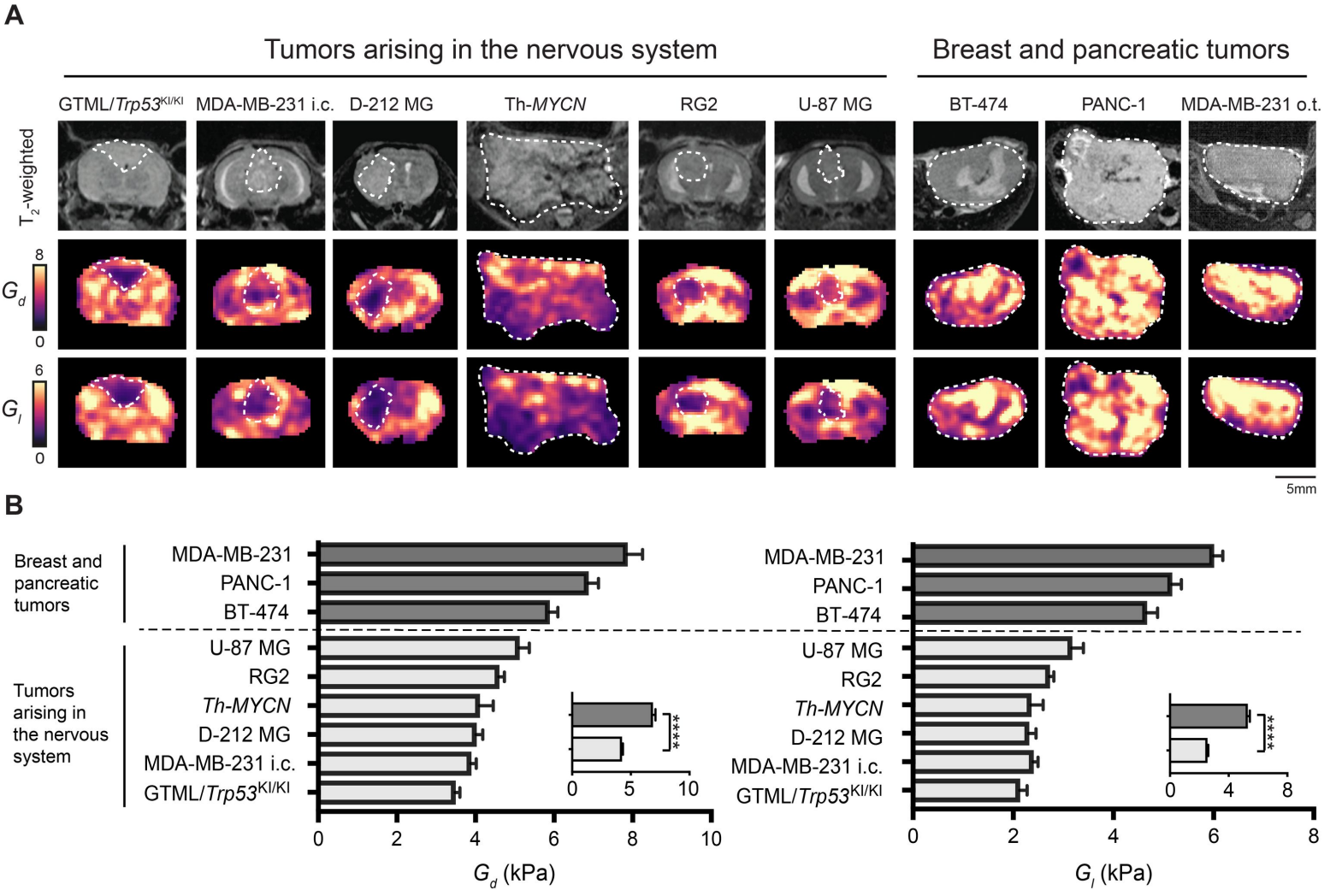
A
Tumors arising in the nervous system
Breast and pancreatic tumors
GTML/Trp53KI/KI
MDA-MB-231 i.c.
D-212 MG
Th-MYCN
RG2
U-87 MG
BT-474
PANC-1
MDA-MB-231 o.t.
T2-weighted
Gd
Gl
8
0
6
0
5mm
B
Breast and pancreatic tumors
Tumors arising in the nervous system
MDA-MB-231
PANC-1
BT-474
U-87 MG
RG2
Th-MYCN
D-212 MG
MDA-MB-231 i.c.
GTML/Trp53KI/KI
****
****
0 2 4 6 8 10
0 5 10
0 2 4 6 8
0 4 8
Gd (kPa)
Gl (kPa)

Figure 2

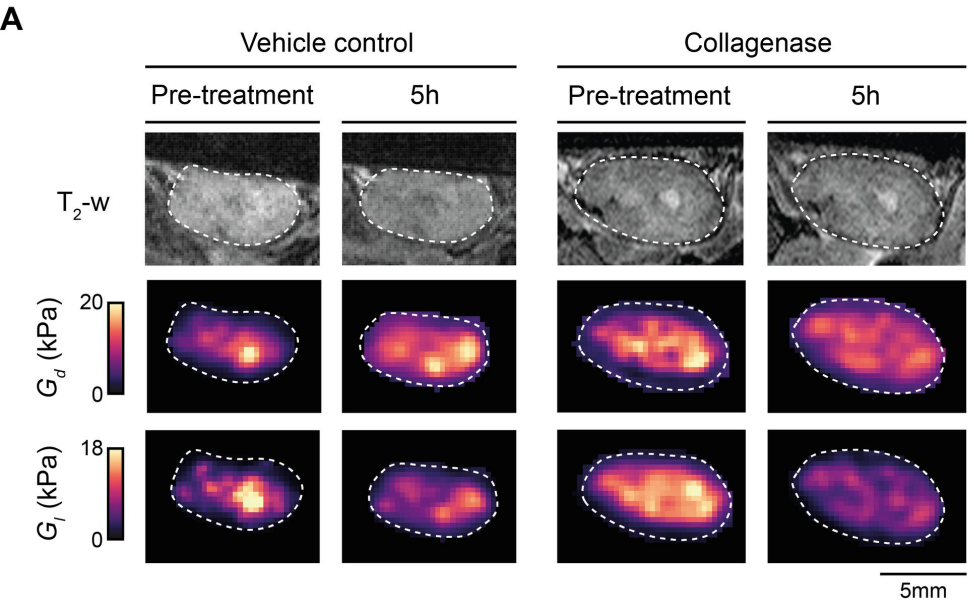
A
Vehicle control
Collagenase
Pre-treatment
5h
Pre-treatment
5h
T2-w
Gd (kPa)
20
0
Gl (kPa)
18
0
5mm

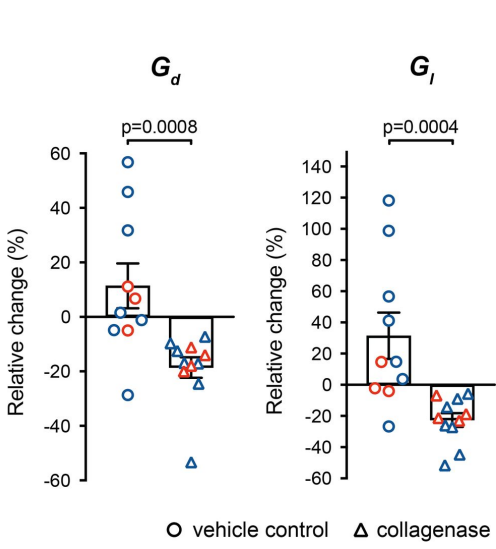
B
Gd
Gl
p=0.0008
p=0.0004
Relative change (%)
60
40
20
0
-20
-40
-60
140
120
100
80
60
40
20
0
-20
-40
-60
vehicle control
collagenase

Figure 3

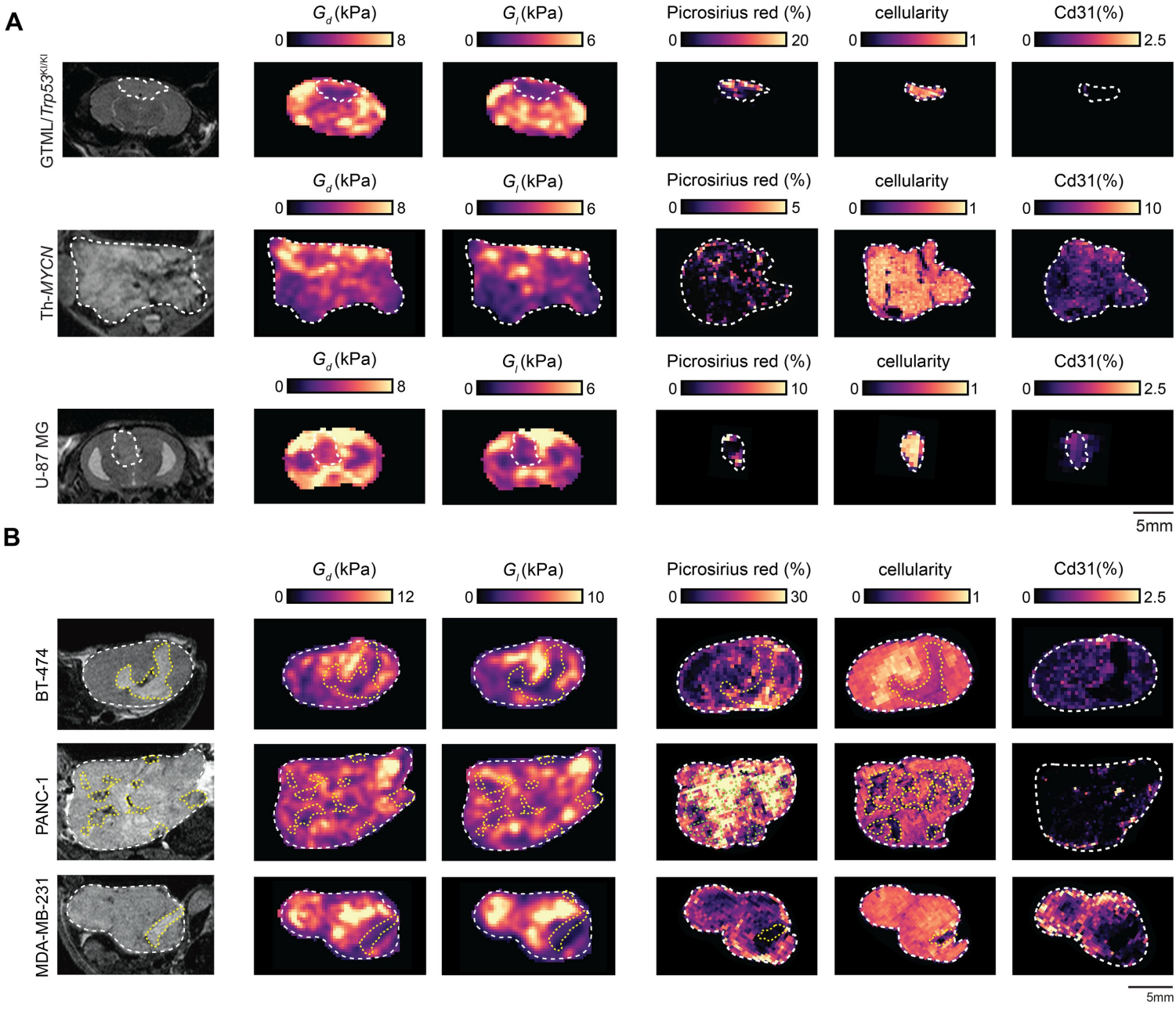
A
G_d(kPa)
G_l(kPa)
Picrosirius red (%)
cellularity
Cd31(%)
GTML/Trp53KI/KI
Th-MYCN
U-87 MG
5mm
B
BT-474
PANC-1
MDA-MB-231
5mm

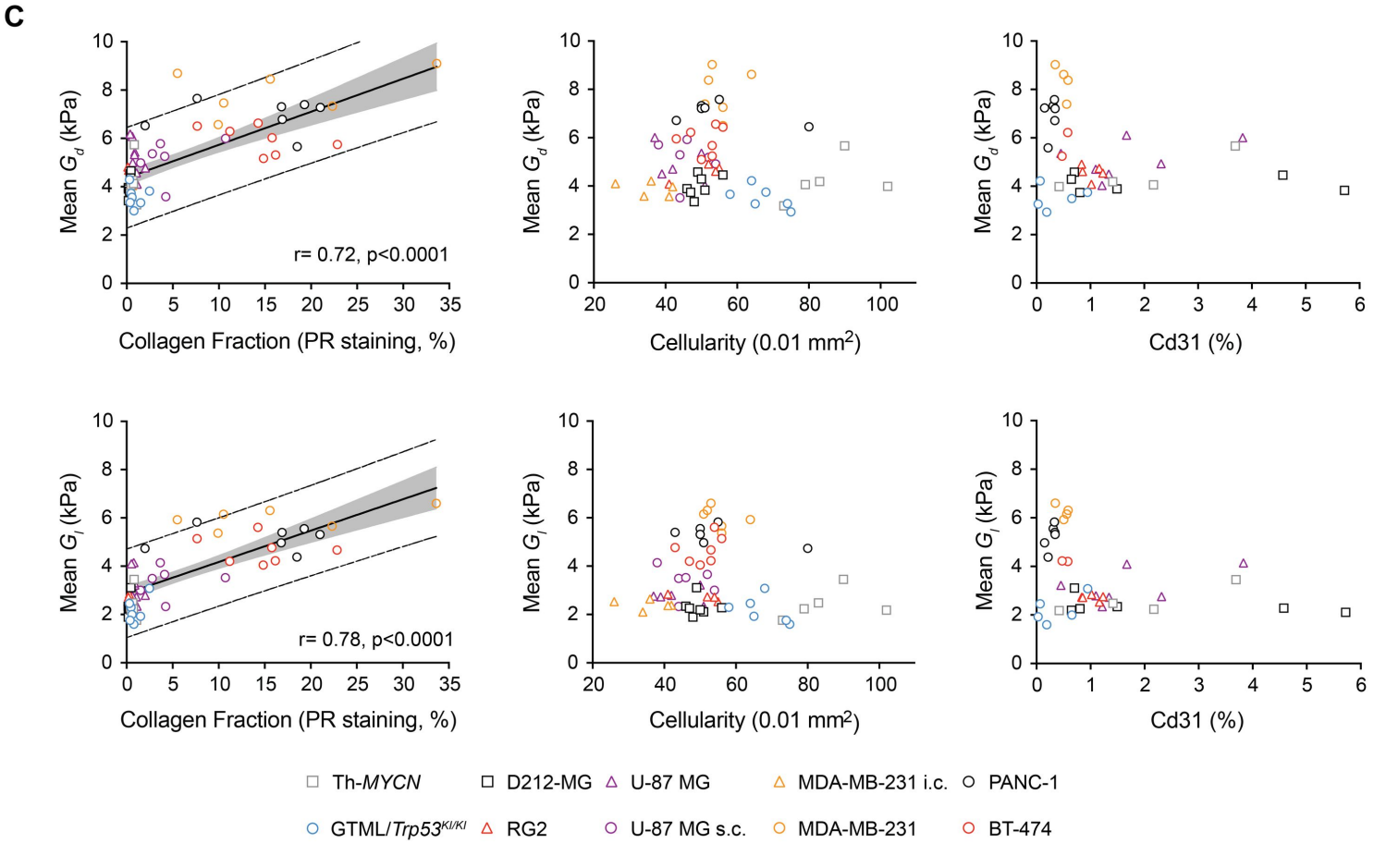
C
Mean G_d (kPa)
Collagen Fraction (PR staining, %)
r= 0.72, p<0.0001
Cellularity (0.01 mm²)
Cd31 (%)
Mean G_l (kPa)
r= 0.78, p<0.0001
Th-MYCN
D212-MG
U-87 MG
MDA-MB-231 i.c.
PANC-1
GTML/Trp53KI/KI
RG2
U-87 MG s.c.
MDA-MB-231
BT-474

Figure 4

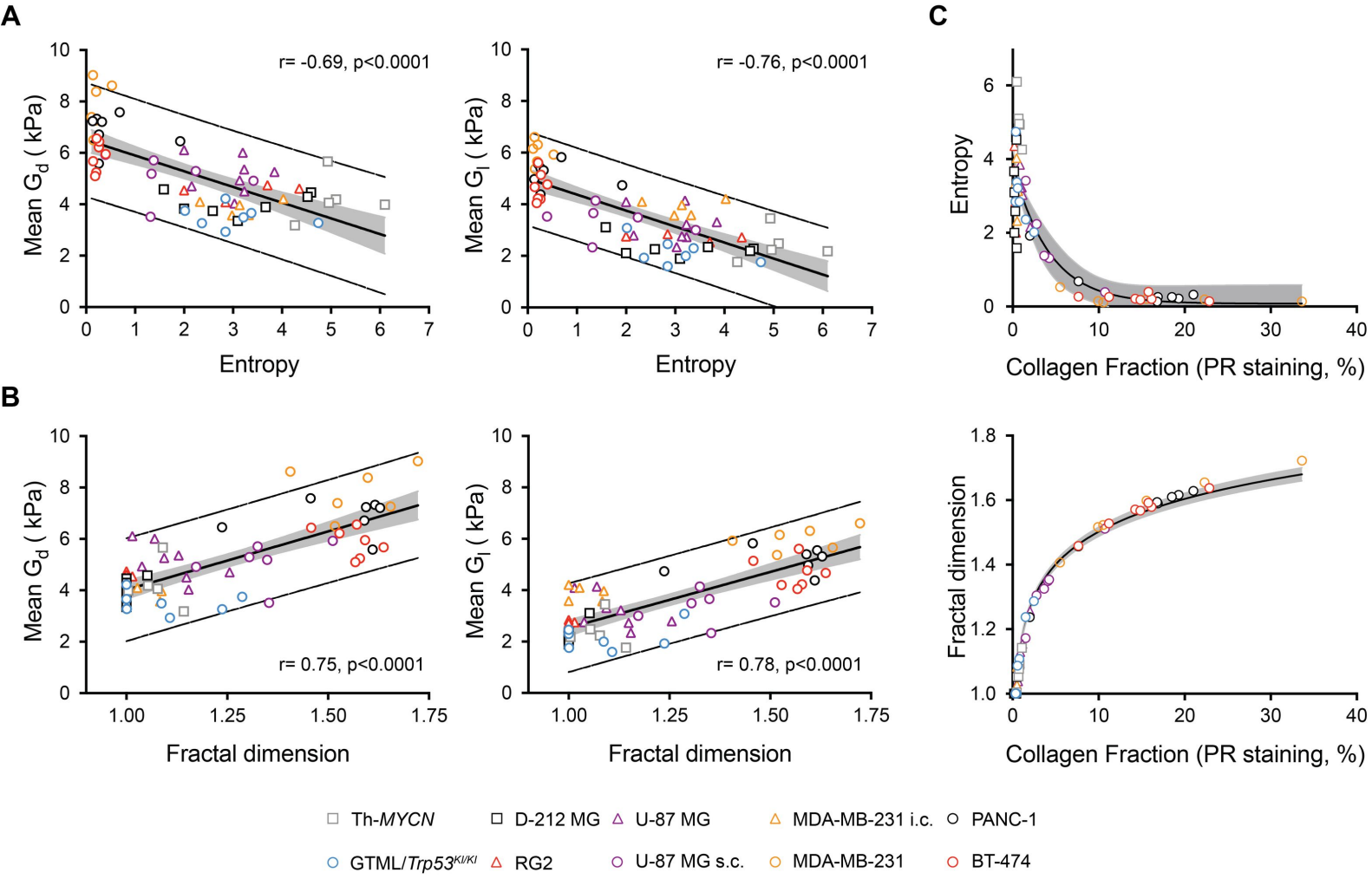
A
B
C
r= -0.69, p<0.0001
r= -0.76, p<0.0001
r= 0.75, p<0.0001
r= 0.78, p<0.0001
Mean G_d (kPa)
Mean G_l (kPa)
Entropy
Fractal dimension
Collagen Fraction (PR staining, %)
Th-MYCN
D-212 MG
U-87 MG
MDA-MB-231 i.c.
PANC-1
GTML/Trp53KI/KI
RG2
U-87 MG s.c.
MDA-MB-231
BT-474